ELSEVIER

Earth and Planetary Science Letters 198 (2002) 77–92

EPSL

www.elsevier.com/locate/epsl

Titanohematite lattice-preferred orientation and magnetic anisotropy in high-temperature mylonites

Jérôme Bascou [a,b,*], M. Irene B. Raposo [b], Alain Vauchez [a], Marcos Egydio-Silva [b]

[a] *ISTEEM, Laboratoire de Tectonophysique, Université de Montpellier II and CNRS, Place E. Bataillon cc49, 34095 Montpellier, France*

[b] *Instituto de Geociências, Universidade de São Paulo, rua do lago, 562, Cep: 05508-900, São Paulo, Brazil*

Received 20 August 2001; received in revised form 7 January 2002; accepted 10 January 2002

Abstract

Magnetic and crystallographic fabric studies were performed in mylonitic granulites from a km-wide strike-slip shear zone in the Ribeira Belt (southeastern Brazil). In these mylonites, a strong compositional layering underlines the tectonic foliation and the elongation of titanohematite, amphibole and orthopyroxene crystals defines a mineral stretching lineation. Magnetic fabric deduced from anisotropy of magnetic susceptibility (AMS) measurements and tectonic fabric compare favorably. Rock-magnetic studies show that both paramagnetic and ferromagnetic minerals can be carriers of AMS. The anisotropy of isothermal remanent magnetization, which is due to the shape-preferred orientation of magnetite grains, is coaxial with AMS. Lattice-preferred orientation (LPO) measurements using the electron backscattered diffraction technique show that orthopyroxene, amphibole, biotite and titanohematite have a strong LPO tightly related to the tectonic fabric. Among these four minerals, titanohematite is the only mineral present in relatively large proportions ($>1.5\%$) in all studied samples. Titanohematite LPO is characterized by a strong concentration of (0001) poles (*c*-axes) sub-perpendicular to the foliation and by a distribution of the poles of the $(2\bar{1}\bar{1}0)$ and $(10\bar{1}0)$ prism planes within the foliation with a maximum close to the lineation. This characteristic LPO is interpreted as resulting from dislocation creep during the mylonitization. Magnetic fabrics and titanohematite LPO fit well: the axis of minimum susceptibility is aligned with the *c*-axis maximum and the axis of maximum susceptibility coincides with the maximum concentration of poles of the prism planes. Titanohematite LPO may provide a valuable constraint for the kinematic interpretation of the magnetic fabrics.

Keywords: lattice; preferred orientation; anisotropy; magnetic susceptibility; electron diffraction analyses; granulites; deformation

1. Introduction

Measurement of anisotropy of magnetic susceptibility (AMS) is a non-destructive and relatively fast technique that allows the retrieval of the magnetic fabric of rocks. It is widely accepted that the AMS fabric usually correlates well with the flow fabric developed during magmatic or solid-state

* Corresponding author. Tel.: +33-467-143602; Fax: +33-467-143603.

E-mail addresses: bascou@dstu.univ-montp2.fr (J. Bascou), irene@usp.br (M.I.B. Raposo), vauchez@dstu.univ-montp2.fr (A. Vauchez), megydios@usp.br (M. Egydio-Silva).

0012-821X/02/$ – see front matter
PII: S0012-821X(02)00475-2

deformation (e.g., [1–3]). Magnetic fabric measurement is then regarded as a reliable method to constrain the kinematics of flow in rocks in which the tectonic structures are difficult to see. However, the AMS fabric may be complex as it results from the combination of all rock-forming mineral contributions. Progress has recently been made in the understanding of the source of magnetic anisotropy through the determination of the anisotropy of remanent magnetization (ARM) fabric in rocks (e.g., [4,5]). ARM is based on the measurement of artificial remanent magnetization [6,7] and makes it possible to isolate the contribution of ferromagnetic minerals to the total magnetic anisotropy.

Strain-induced lattice-preferred orientation (LPO) of minerals in deformed rocks is commonly used to constrain the mechanical behavior of minerals and to study the kinematics of deformation (e.g., [8,9]). The relationships between crystallographic and magnetic preferred orientations have been investigated by various authors (e.g., [10–13]). However, these investigations have been focused on silicate phases. Few studies deal with iron oxides, although they are often the dominant source of susceptibility. LPOs of hematite ores from the Quadrilátero Ferrífero (Brazil) have been measured by Hrouda et al. [14] using optical and X-ray goniometry techniques, and by Brokmeier [15] and Will et al. [16] using neutron diffraction technique. AMS measurements have been recently performed by Siemes et al. [17] on samples from the same area. These studies together show that both the concentration of *c*-axes of hematite and the minimum axis of magnetic susceptibility are close to the pole of the tectonic foliation. However, in the case of polyphase specimens, X-ray and neutron diffraction techniques are limited and extremely time-consuming (see [18] for discussion). Recent developments of the electron backscattered diffraction (EBSD) technique in the domain of earth sciences (e.g., [19]) allow the measurement of mineral LPOs in polyphase samples with grain size ≥ 1 μm, even for opaque and low-symmetry minerals.

Kinematic studies in high-grade metamorphic terranes are of primary importance because they may allow tectonic processes active in the middle and lower crust to be recognized. However, due to pervasive recrystallization and annealing in these rocks, lineations and foliations are often difficult to observe and measure. Magnetic anisotropy studies in granulitic terranes may circumvent this difficulty. Thus, the relationships between magnetic fabrics and LPO of rock-forming minerals must be understood in order to constrain the tectonic signature of magnetic fabrics of high-temperature rocks.

To better constrain these relationships we have:(1) determined the anisotropies of magnetic susceptibility and of remanent magnetization for samples from five sites within a granulitic shear zone; (2) measured the LPOs of the major silicate and iron oxide phases in these mylonites; (3) compared the magnetic fabric, LPOs, and finite-strain axes of these tectonites.

2. Geological setting and petrology of samples

The Ribeira belt [20] stretches over more than 1000 km along the southeastern coast of Brazil (Fig. 1). This belt is regarded as resulting from the convergence between the São Francisco and Congo cratons at the end of the Gondwana assembly [21]. In the central part of the Ribeira belt, the deformation results from a continuous tectonic evolution during which two main regimes have successively prevailed (e.g., [22]): early thrusting and nappe emplacement toward the São Francisco craton, i.e., toward the continent, followed by development of dextral transcurrent faults under slightly retrogressive conditions (from 807–877°C at 0.6–0.7 GPa, to 734–743°C at 0.5 GPa [23]). This orogenic event remobilized 2.2 Gyr old gneissic terranes [24]. The peak of metamorphism was dated at 575 ± 20 Ma [25,26]. Synkinematic *P–T* conditions decrease progressively southwestward, from granulitic to upper greenschist facies in the southernmost part of the Ribeira belt. Metamorphic and tectonic evidence agrees with a transpressional deformation. Finite-element modeling [22] suggests that the initiation of the shear zones and the NE–SW variation in erosion level may have been induced by the indentation of the SE termination of the São Francisco craton.

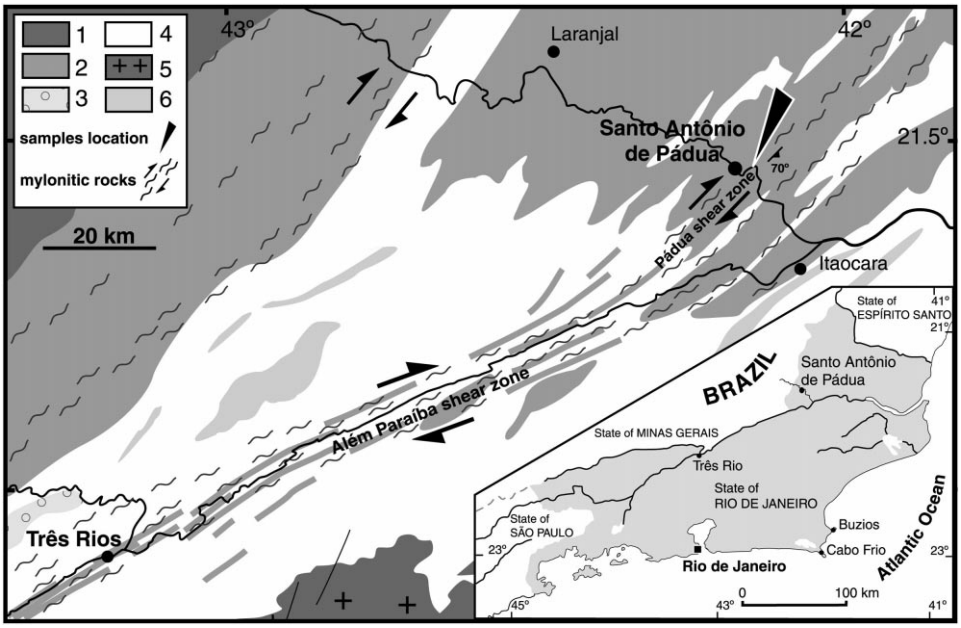

Fig. 1. Schematic geologic map of the Além Paraíba–Pádua shear zone showing the location of the studied samples. (1) Polycyclic basement; (2) granulites and charnockites (Juiz de Fora complex); (3) enderbites; (4) gneisses and migmatites (Paraíba do sul complex); (5) syntectonic granites; (6) marbles (Italva group).

The samples used in this study have been collected in the Pádua shear zone (Fig. 1), which belongs to a larger transcurrent shear zone system (the Além Paraíba–Pádua Shear System) developed in the central domain of the Ribeira belt [27]. In the Pádua shear zone, mylonitic zones several kilometers wide display a pervasive foliation (N040E–70SE) characterized by a compositional layering and a sub-horizontal mineral stretching lineation marked by elongated crystals or mineral aggregates (orthopyroxene, amphibole, feldspar, titanohematite) and boudinage. Asymmetric boudins and mantled feldspar porphyroclasts indicate a dextral sense of shear. Five representative sites characterized by a penetrative deformation at the macroscopic scale have been selected. Four mylonite samples (RB609A, RB538, RB607A, and RB540) display a clear lineation and one (RB614), collected 6 km away from others, comes from a mylonitic zone where no clear lineation was observed macroscopically. The mineralogy of the studied samples consists mainly of quartz, plagioclase (An_{20} to An_{40}), K-feldspar, biotite, and orthopyroxene and/or amphibole in variable proportions. The microstructure is characterized by alternating, almost monomineralic layers of rectangular quartz crystals or equidimensional recrystallized feldspar grains. The fine-grained (down to 120 μm) feldspar-rich layers contain deformed plagioclase and K-feldspar porphyroclasts (up to 300 μm).

All samples include opaque minerals in proportion ranging from 2% (RB614) to 9.5% (RB609A). Reflected-light observations and quantitative analyses using scanning electron microscope (SEM) connected to an X-ray energy dispersive spectrometer (EDS) indicate that the opaque minerals mostly belong to the hematite–ilmenite solid solution. The complete hematite–ilmenite solid solution is conventionally known as titanohematite ($x\mathrm{FeTiO_3}$-$(1-x)\alpha\mathrm{Fe_2O_3}$) in the rock magnetism literature. The studied samples contain mainly Ti-rich titanohematite close to the ilmenite end-member. The grains either are relatively homogeneous, with thin exsolution lamellae, or display wide lens-shaped exsolutions of Ti-poor titanohematite (ilmeno-hematite or hemoilmenite). Titanohematite grains are strongly elongated parallel

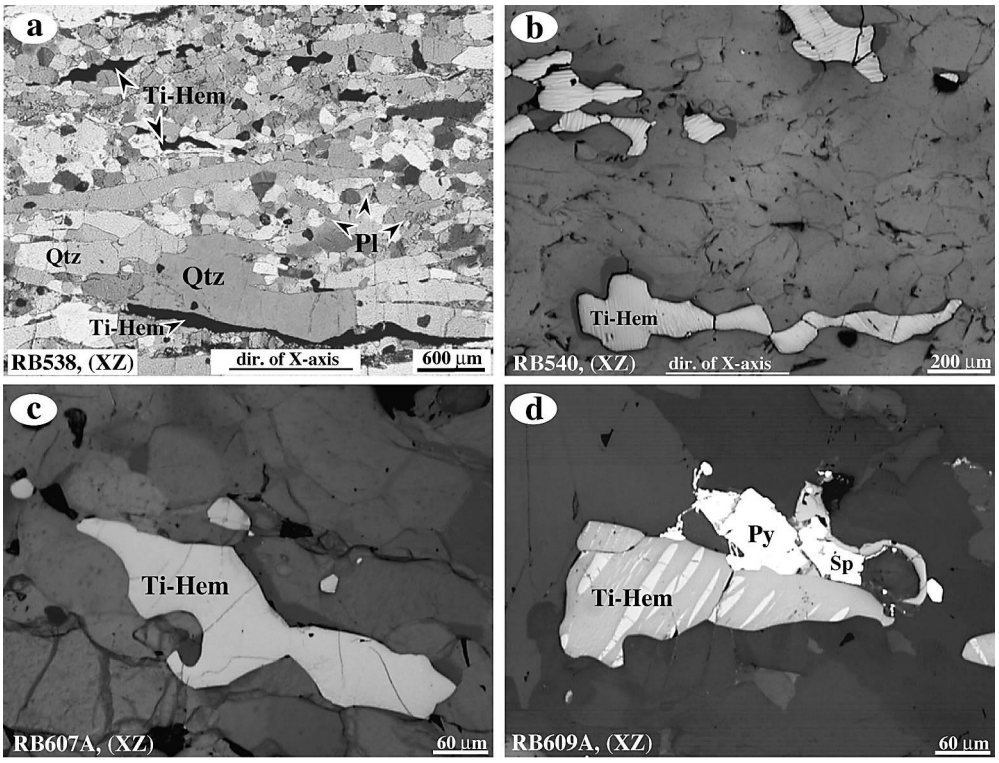

Fig. 2. Photomicrographs showing typical elongated titanohematite grains (Ti-Hem). (a) Typical microstructure of mylonites with polycrystalline quartz ribbons, recrystallized feldspar and elongated titanohematite grains; partially crossed nicols. (b) Titanohematite grains showing thin exsolution lamellae. (c) Ti-rich titanohematite grain without lamellae. (d) Titanohematite showing wide exsolution lenses of Ti-poor titanohematite. Sulfides are represented by pyrite (Py) and sphalerite (Sp). Thin sections parallel to the *xz* structural plane; b–d in reflected light.

to the lineation (Fig. 2); their width is on average 50–100 μm and their length is variable (up to 1 mm). Sample RB538 presents the more elongated titanohematite grains with shape ratio >7. Some samples also contain micrometric inclusions and/or thin exsolutions of magnetite. Sulfides, especially pyrite (the most abundant), chalcopyrite, sphalerite and a minor amount of pyrrhotite are also present. They generally replace the Ti–Fe oxides and do not display any shape-preferred orientation.

3. Magnetic measurements

3.1. Magnetic mineralogy and rock magnetism

To determine the magnetic minerals responsible for the magnetic anisotropy in the studied sites, several rock-magnetic experiments were carried out: (a) thermomagnetic curve determinations, (b) coercivity spectra from both anhysteretic remanence and alternating field (AF) demagnetization, (c) thermal demagnetization, (d) isothermal remanent magnetization (IRM) acquisition, and (e) hysteresis measurements.

Thermomagnetic curves were obtained in bulk rock from at least two specimens from each site. The experiments were performed by measuring the susceptibility changes with temperature under Ar atmosphere conditions using Kappabridge instruments (KLY-CS3 and KLY-CS3L, Agico, Czech Republic). In addition, we obtained thermomagnetic curves on concentrated ferromagnetic mineral separates from the specimens from three sites (Fig. 3A). All ferromagnetic mineral

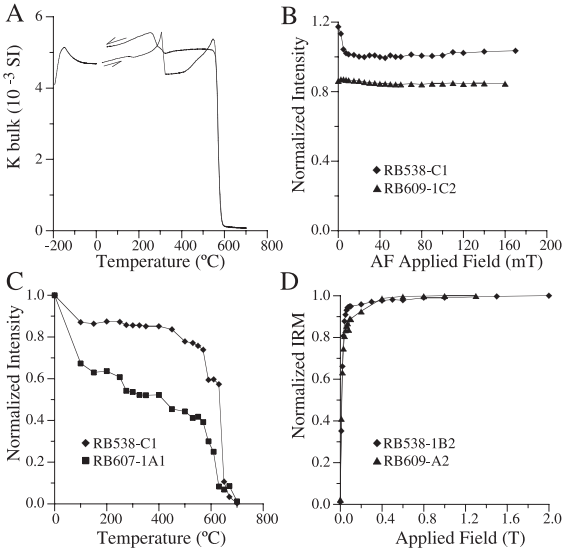

Fig. 3. (A) Representative thermomagnetic curves on ferromagnetic mineral concentrate from specimens RB607. (B) Normalized intensity of magnetization curves versus AF obtained during the AF tumbling demagnetization process. (C) Normalized intensity of magnetization curves versus temperature obtained during the thermal demagnetization process. (D) Examples of isothermal remanent acquisition curves.

concentrations exhibit K–T curves with a Hopkinson peak and a sharp decrease in susceptibility. A well-defined pick was observed around −150°C that probably indicates the Verwey transition, characteristic of almost pure magnetite. The high-T susceptibility experiments show a steep decrease in the intensity of susceptibility at temperatures near 580°C and around 320°C (Fig. 3A), which indicate (titano)magnetite and pyrrhotite, respectively. It is worth noting that pyrrhotite was observed thermomagnetically only in specimens from site RB607 among the analyzed sites.

Coercivity spectra were determined by subjecting samples to stepwise AF demagnetization in a Molspin tumbling demagnetizer (Molspin, Newcastle-upon-Tyne, UK) by fields up to 100 mT. Some samples were demagnetized by fields up to 170 mT using a automated three-axis AF demagnetizer coupled to the cryogenic magnetometer. The samples were also subjected to stepwise thermal demagnetization using a non-inductive Schonstedt thermal demagnetizer. The coercivity spectra determined from both anhysteretic remanence [28], and AF demagnetization (Fig. 3B) show that the analyzed samples have both low (<30 mT) and high coercivity. The thermal demagnetization (Fig. 3C) shows blocking temperatures in ranges of 300–350°C, 450–590°C and 600–670°C. These blocking temperatures are coherent with a mixture of pyrrhotites (sample RB607), (titano)magnetite and titanohematite, and suggest a similar contribution of both (titano)magnetite and titanohematite to remanence and AMS. IRM experiments carried out using a pulse magnetometer (MMPM9, Magnetic Measurements) show that the samples reached their complete saturation around 1–1.2 T (Fig. 3D). Saturation in such high fields indicates the presence of titanohematite, as suggested by coercivity and blocking temperature spectra.

Hysteresis measurements at room temperature were performed on at least three samples per site using a vibrating sample magnetometer (VSM-Nuvo, Molspin, Newcastle-upon-Tyne, UK) in fields up to 1 T. Some typical hysteresis curves are reported in Fig. 4. The curves are symmetrical in all cases. For the majority of the samples, the shape of the hysteresis curve reveals that ferromagnetic grains carry most of the bulk susceptibility. However, they also show that there is a significant contribution of the paramagnetic minerals to the bulk susceptibility as shown by the high-field part of the hysteresis (RB607, RB609, and RB614). Even though it cannot be excluded that the high-field part of the hysteresis is due to the ferromagnetic titanohematite instead of paramagnetic minerals since samples reach the saturation in fields >1 T (Fig. 3D) which is higher than maximum VSM applied field (1 T).

3.2. Anisotropy of low-field magnetic susceptibility (AMS) and magnetic fabrics

AMS is the tensor which relates the intensity of the applied field (H) to the acquired magnetization (M) of a material through the equation: $M_i = K_{ij} H_j$, where K_{ij} is a symmetrical second-rank tensor referred to as the susceptibility tensor [1]. The susceptibility tensor is expressed by its principal eigenvalues (susceptibility magnitudes) and eigenvectors (their orientations), $K_{max} \geq K_{int} \geq K_{min}$ representing the maximum, in-

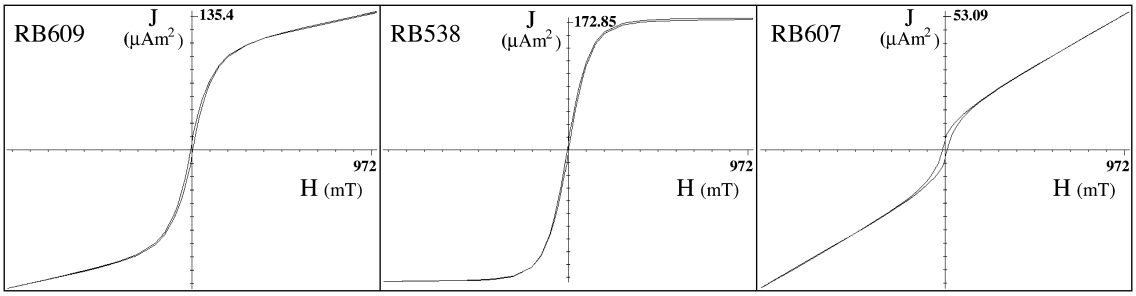

Fig. 4. Hysteresis loops for the specimens from analyzed sites. J = magnetization and H = applied field.

termediate, and minimum axes of susceptibility, respectively. AMS describes the variation of magnetic susceptibility with direction within a material, and represents the contributions of all rock-forming minerals (i.e., dia-, para- and ferromagnetic). The K_{max} axis represents the magnetic lineation while K_{min} is the pole of the magnetic foliation (the plane containing K_{max} and K_{int} axes).

AMS measurements were performed on 2.5×2.2 cm cylindrical specimens, cut from the oriented cores drilled with a gas-powered portable drill in the sampling sites. At least three specimens from each core were cut. A total of 60 specimens were measured using the KLY-3S Kappabridge (Agico, Czech Republic). AMS data are presented in Table 1. The mean magnetic susceptibility, expressed by $K_m = (K_{max}+K_{int}+K_{min})/3$ in SI units, is generally higher than 10^{-3} SI with an average of 10.68×10^{-3}. The anisotropy degree, given by $P_{AMS} = K_{max}/K_{min}$, is high ($1.510 \leq P_{AMS} \leq 5.543$). There is no clear relationship between K_m and P_{AMS} (Table 1). Jelinek's [29] parameter T_{AMS} ($T_{AMS} = (\ln F_{AMS} - \ln L_{AMS})/(\ln F_{AMS} + \ln L_{AMS})$ where $F_{AMS} = K_{int}/K_{min}$ and $L_{AMS} = K_{max}/K_{int}$) shows that the magnetic susceptibility ellipsoids are oblate ($T_{AMS} > 0$, Table 1 and Fig. 5).

The mean AMS eigenvectors (K_{max}, K_{int} and K_{min}) and the 95% confidence cone for each site were calculated using the bootstrap method of Constable and Tauxe [30]. For each site, these eigenvectors are generally well grouped with low values for the 95% confidence cones. The AMS analysis at the site scale defines the fabrics shown in Fig. 6A. Since both para- and ferromagnetic minerals are present, the AMS is due to a combination of the preferred crystallographic orientations of titanohematite and paramagnetic matrix minerals, and to the shape anisotropy of magnetite grains.

3.3. ARM and ARM fabrics

ARM was determined through isothermal remanent magnetization (AIRM; see [6,7] for a review). AIRM measurements were performed using a pulse magnetometer. The procedure involves

Table 1
AMS data

Site	*u.c.*	K_m	Mean AMS parameters			
		(10^{-3} SI)	L_{AMS}	F_{AMS}	P_{AMS}	T_{AMS}
RB538	12	21.52	1.402	3.955	5.543	0.604
RB540	11	10.70	1.174	1.325	1.557	0.270
RB607	12	3.46	1.118	1.342	1.510	0.450
RB609	14	14.52	1.156	1.342	1.551	0.332
RB614	11	3.18	1.058	1.711	1.810	0.811
Means		10.68	1.182	1.935	2.394	0.493

u.c. = number of specimens measured. The mean susceptibility K_m, the lineation L_{AMS}, the foliation F_{AMS} and Jelinek's parameter T_{AMS} are defined in the text.

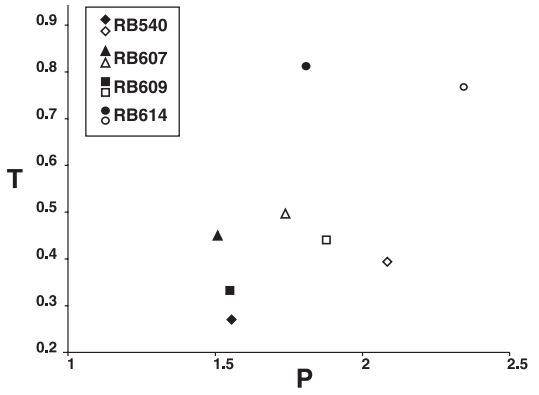

Fig. 5. *P* versus *T* (Jelinek's parameter) plot. Black symbols = AMS parameters; white symbols = AIRM parameters. Site RB538 was not included in the figure (see text for explanation).

applying a magnetic field for a short period of time, measurement, and demagnetization along different positions for each specimen. For each position, the IRM is determined as the difference between a remanence magnetization base level and the remanence measured after IRM acquisition. After the measurement and before IRM acquisition in other positions, the specimen must be demagnetized to eliminate the previously imposed magnetization. Six different measurement positions were used since this scheme has proved to be sufficient to calculate the IRM tensors in this study. Before AIRM analysis, samples were demagnetized by AF tumbling at 100 mT to establish the base level. For AIRM determinations the IRM was acquired applying a magnetic field of 20 mT, which was further removed by an AF tumbling demagnetization field of 30 mT (see [28] for discussion). This procedure was repeated for the other positions and the AIRM tensor was calcu-

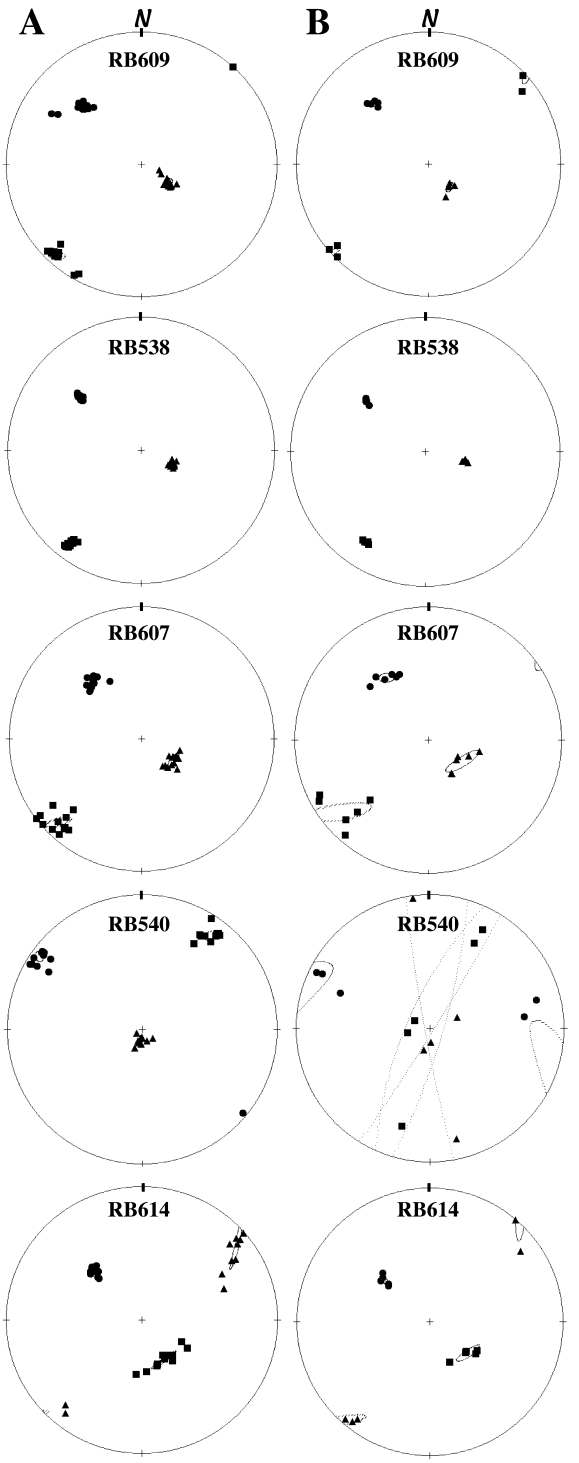

→

Fig. 6. Magnetic fabrics determined (A) from anisotropy of low-field magnetic susceptibility (AMS) and (B) from anisotropy of isothermal remanent magnetization (AIRM). Squares = maximum susceptibility and remanence (K_{max}, $AIRM_{max}$), triangles = intermediate susceptibility and remanence (K_{int}, $AIRM_{int}$) and circles = minimum susceptibility and remanence (K_{min}, $AIRM_{min}$). Dashed line ellipses = 95% confidence ellipses. Equal-area, lower hemisphere projections, in the geographical horizontal plane.

lated by the least-squares method, which showed root-mean-squares $< 5\%$.

As usually observed [6], the anisotropy degree ($P_{AIRM} = AIRM_{max}/AIRM_{min}$) is more pronounced than P determined from AMS (Fig. 5). RB538 has the strongest magnetic anisotropy. This site is characterized by a very strong P_{AMS} value ($P_{AMS} = 5.543$) and an extreme P value ($P_{AIRM} = 17.841$). The ellipsoid shapes are oblate ($0.393 \leq T_{AIRM} \leq 0.767$) in agreement with AMS results (Fig. 5).

The eigenvectors ($AIRM_{max} > AIRM_{int} > AIRM_{min}$) are usually well grouped except for RB540 in which only one eigenvector ($AIRM_{min}$) has been defined (Fig. 6B). The statistical evaluation followed the bootstrap method [30] originally developed for AMS studies. AIRM has a distinct advantage over AMS because its fabric is exclusively given by the ferromagnetic minerals. Since titanohematite has a high coercivity (> 100 mT), AIRM only measures the contribution of magnetite. Therefore eigenvectors of the AIRM tensors (Fig. 6B) indicate the shape-preferred orientation of the magnetite grains. The measured AIRM fabrics are coaxial with AMS fabrics.

4. Crystallographic fabric

4.1. LPO determination

LPOs were measured using a scanning electron microscope JEOL JSM 5600 through indexation of EBSD [31,32]. Kikuchi bands, which compose the diffraction patterns, are generated by the interaction of a vertical incident electron beam with a planar crystal surface. We used 10 cm^2 ultrapolished thin sections, tilted at 70° from horizontal. A phosphor screen collects the backscattered electrons and gives a photonic image of the EBSD pattern. A low-light, high-resolution digital camera records this photonic image that is then processed and indexed using the CHANNEL+ software (HKL technology). At each point of measurement, the Euler angles ($\varphi 1$, ϕ, $\varphi 2$) characterizing the orientation of the crystal lattice are determined with a precision better than 1° [33].

Automatic orientation mapping was not possible due to the large contrast in mean atomic number between silicate and oxide phases, and to the large variety of mineralogical phases that compose these rocks. Thus lattice orientation of silicate and oxide phases was measured grain-per-grain on the whole surface of the thin sections. We first tested the influence of compositional variations in the hematite–ilmenite series on the indexation of diffraction patterns. The indexation of titanohematite using a set of the 75 strongest reflection bands calculated using either the 'hematite structure' (space group = $R\bar{3}c$) or the ordered 'ilmenite structure' (space group = $R\bar{3}$) yields similar results.

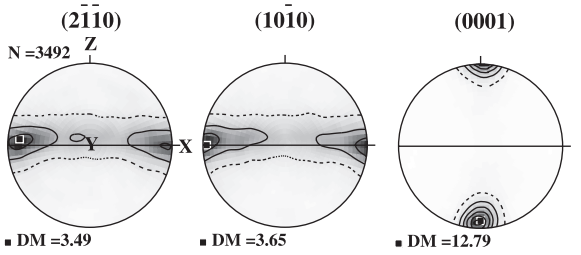

Fig. 7. Hemalite LPO of typical iron ores from the Quadrilátero Ferrífero. Automatic EBSD measurement with a 200 μm step. Analyzed thin section cut parallel to the *xz* structural plane. Crystallographic orientations projected on equal-area, lower hemisphere in the *x,y,z* structural frame. Foliation (*xy* plane, full line) is vertical E–W and the lineation (*x*) is horizontal in the foliation plane. Contours by 1% area for (2$\bar{1}\bar{1}$0) and (10$\bar{1}$0) poles, and at 2, 4, 6% etc. by 1% area for (0001) poles. N = number of measurements and DM = maximum density.

In order to validate this approach, we have measured the LPO of an intensely deformed hematite ore from the Quadrilátero Ferrífero in Minas Gerais (Brazil) that is characterized by a typical lepidoblastic microtexture [34]. For this specific sample, the hematite LPO has been measured using the EBSD automatic measurement procedure. The LPO (Fig. 7) is characterized by the *c*-axes strongly concentrated close to the normal to the foliation, and by the poles of prism planes (2$\bar{1}\bar{1}$0) and (10$\bar{1}$0) concentrated close to the lineation. This LPO presents a good agreement with those obtained on hematite ores of the Quadrilátero Ferrífero using texture goniometry and, for the *c*-axis, using reflected-light microscopy [14–16].

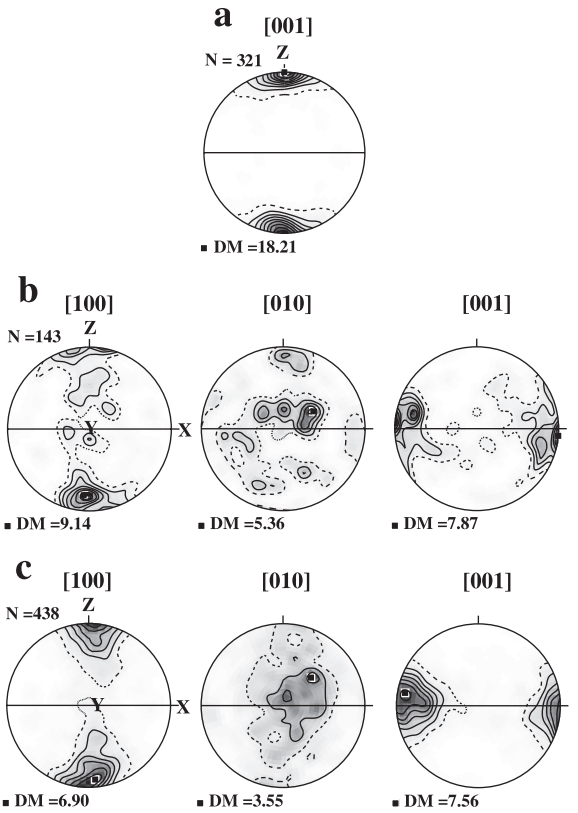

Fig. 8. Typical LPO in mylonites from the Além Paraíba–Pádua shear system. (a) Biotite, sample RB614. (b) Orthopyroxene, sample RB607A. (c) Amphibole, sample 609A. EBSD measurements. Contours at 1, 3, 5% for a and at 1, 2, 3% for b and c by 1% area. Projection and labels as in Fig. 7.

4.2. Results

Microstructures and LPOs of the main silicates in mylonites outcropping in the Além Paraíba–Pádua shear system are described in detail in [27] and are interpreted as resulting from high-temperature deformation and extensive annealing. Except for the quartz LPO that shows a complex distribution likely due to post-kinematic annealing, the LPO of silicates is tightly correlated with the tectonic fabric (*x*-, *y*- and *z*-axes). The LPO of plagioclase is characterized by [100] axes parallel to the *y*-axis and (010) poles normal to the foliation, and some samples display a submaximum (010) close to the lineation X [35]. The LPO of biotite (Fig. 8a) is characterized by the *c*-axes parallel to the *z*-axis. The LPO of orthopyroxene and amphibole (Fig. 8b,c) shows (100) poles concentrated close to *z*, [010] axes close to *y*, and [001] axes close to *x*.

Among the Fe–Ti oxides, deformed titanohematite is largely dominant. Magnetite is difficult to observe in reflected light since it appears in micro-domains (a few μm in size), included in elongated titanohematite grains. The number of diffraction patterns indexed as magnetite (spinel structure) in micro-domains varies from sample to sample but is generally lower than 90 among a total larger than 900 crystals (silicates and iron oxides) indexed. LPO of magnetite determined from these diffraction patterns is very weak; magnetite is almost randomly oriented. Fig. 9 shows the strongest magnetite LPO measured. The [100] axis is characterized by numerous concentrations distributed on the whole hemisphere, and the maximum density (DM = 3.04) is located at ca. 40° of the lineation. The [111] and [110] axes are almost randomly oriented. In contrast, titanohematite displays a strong LPO characterized by (0001) poles (*c*-axes) concentrated normal to the foliation. The poles of the prism planes $(2\overline{1}\overline{1}0)$ and $(10\overline{1}0)$ tend to form a girdle parallel to the foliation, which contains a maximum close to the lineation (Fig. 10a,b). Fig. 10c shows a representative inverse pole figure calculated for sample RB607A. The pole of the foliation (*z*) is strongly concentrated parallel to the *c*-axis and the lineation is scattered in the basal plane with weak maximum close to the poles of the prism planes. This LPO of titanohematite is typical of basal slip in trigonal minerals (such as quartz for instance). Similar LPO patterns have been described for ilmenite in a gabbroic shear zone by Agar and Lloyd [36] and are interpreted as resulting from

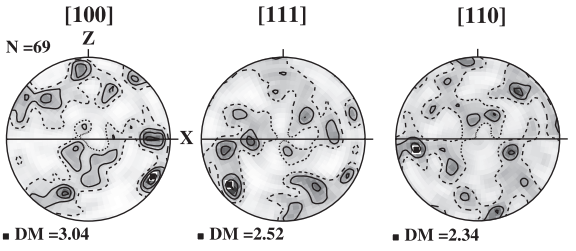

Fig. 9. Magnetite LPO of sample RB538. Contours at 1, 1.5, 2% by 1% area. Projection and labels as in Fig. 7.

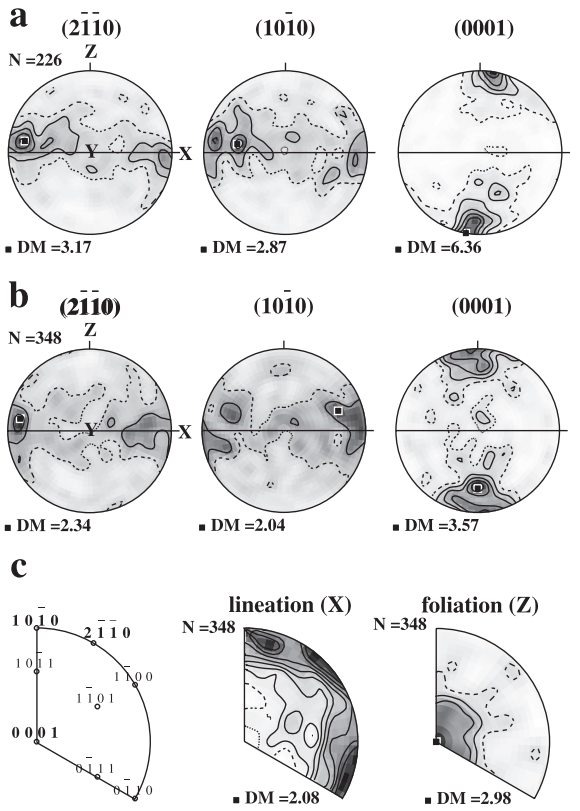

Fig. 10. Titanohematite LPO. (a,b) Pole figures for samples RB609A (a) and RB607A (b). Contours at 1, 1.5, 2, 2.5, 3% etc. by 1% area for (2$\bar{1}\bar{1}$0), (10$\bar{1}$0) poles, and at 1, 2, 3% etc. by 1% area for (0001) poles for a. Contours at 1, 1.5, 2, 2.5, 3% etc. by 1% area for b. Projection and labels as in Fig. 7. (c) Inverse pole figures for sample RB607A showing the projection of lineation (x) and the pole of the foliation (z) in the crystallographic reference frame (upper-hemisphere projection). Contours at 0.2, 0.4, 0.6% etc. by 1% area for the lineation and at 1, 1.5, 2, 2.5, 3% etc. by 1% area for the foliation. A reference plot showing the poles of crystallographic planes is displayed on the left.

dislocation creep. Dislocation glide on the basal plane, followed by grain boundary migration and anisotropic grain growth, was invoked to explain the development of the strong hematite LPO (e.g., Fig. 7) in naturally deformed hematite from the Quadrilátero Ferrífero [37]. Experimental deformation of fine-grained hematite [38] shows that strain accommodation through dislocation glide on (0001) increases for temperatures above 700°C. Basal slip was also observed during high-temperature experimental deformation of synthetic corundum [39]. At low temperature, microfracturing, twinning on r{10$\bar{1}$1} and (0001), and prismatic slip {a} ⟨m⟩ from 200°C, are the main deformation mechanisms [40,41].

In conclusion, since titanohematite grains are elongated parallel to the macroscopic lineation and its measured LPO displays a simple and consistent correlation with the tectonic fabric, we suggest that titanohematite LPO results from dislocation creep during high-temperature plastic deformation. The good correlation of the titanohematite LPO with the LPO of the main silicate minerals (orthopyroxene, amphibole and plagioclase) strengthens this interpretation.

5. Comparison between magnetic and crystallographic fabric

To allow comparison, magnetic, crystallographic and tectonic fabrics for all samples have been plotted in geographic coordinates (Fig. 11). To compare the LPOs with the principal mean susceptibility axes, the eigenvalues and eigenvectors of the normalized orientation tensors [42] were calculated from LPOs. The best axis is given by the eigenvector of the largest eigenvalue, and the pole to the best plane by the smallest one. In addition, the fabric strength is expressed by the dimensionless texture index J [43], which ranges between 1 (random LPO) and infinity (single crystal). In our calculations, the J index has an upper bound of ca. 250 due to truncation at degree 22 of the spherical harmonic series expansion.

As already stated, AMS represents the sum of the para-, dia- and ferromagnetic contributions. Ferromagnetism is mainly carried by iron oxides (mostly Ti-poor titanohematite and magnetite). Magnetite has a very high susceptibility (>2 SI) and a very low magnetocrystalline anisotropy [3]; its AMS is controlled dominantly by the grain shape (e.g., [44,45]). In the studied samples, titanohematite shows compositional variations. SEM-EDS analyses show that most grains are Ti-rich titanohematite close to the ilmenite end-member with exsolutions of Ti-poor titanohematite close to the hematite end-member. The mean susceptibility reported for hematite ranges be-

tween 2×10^{-3} and 8×10^{-2} SI [34]. Hematite has a very high intrinsic crystallographic magnetic anisotropy with the direction of maximum susceptibility in the basal plane and the direction of minimum susceptibility along the *c*-axis; its anisotropy degree (*P*) is frequently greater than 100 [46]. Paramagnetic minerals are mostly represented by Ti-rich titanohematite orthopyroxene, amphibole and biotite; their AMS is due to their magnetocrystalline anisotropy (e.g., [7]). EBSD measurements show that orthopyroxene, amphibole, biotite and titanohematite have a strong LPO tightly correlated with the tectonic fabric. Among these minerals, titanohematite is the only ubiquitous mineral and its volume fraction is relatively large ($>1.5\%$). We have therefore focused on the comparison between the LPO of titanohematite and the magnetic fabric.

The minimum susceptibility axis (K_{min}) of the ASM fabric, the best *c*-axis of titanohematite (Fig. 11), and the pole of the macroscopic foliation plane (p in Fig. 11) are close to each other. The maximum concentrations of $(2\bar{1}\bar{1}0)$ and $(10\bar{1}0)$ poles in the well-lineated samples RB609A, RB538, RB607A and RB540, although relatively weak, lie close to the maximum susceptibility axis (K_{max}). The best axis (E1, Fig. 11) of $(2\bar{1}\bar{1}0)$ and $(10\bar{1}0)$ prism planes and K_{max} are almost parallel to the lineation (l in Fig. 11). These relationships between K_{min}, K_{int} and K_{max} and the LPO of titanohematite are consistent with relationships given by Uyeda et al. [46] for the hematite and ilmenite–hematite single crystal (i.e., (K_{max}, K_{int})$\parallel$the basal plane, and $K_{min}\parallel$[0001]). For RB614, which displays no clear lineation although the foliation is well-marked, [0001] is strongly concentrated normal to the foliation, and the $(2\bar{1}\bar{1}0)$ and $(10\bar{1}0)$ poles are scattered in the foliation plane. Fig. 6A shows that the axes of minimum susceptibility defined for RB614 are strongly concentrated parallel to the best *c*-axis and close to the pole of the macroscopic foliation plane (Fig. 11), whereas the axes of both intermediate and maximum susceptibility tend to form a girdle within the foliation plane. For sample RB614, AIRM fabric (Fig. 6B) shows a concentration of the axes of maximum remanence that contrasts with the dispersion of the maximum susceptibility axes (Fig. 6A). AIRM was not measured for all specimens for which AMS was measured (5 and 11 specimens, respectively) and this may impede any detailed comparison. In addition, the axes [001] of amphibole (~7 vol%) tend to be scattered in the foliation plane (Fig. 12) and present a clear maximum of concentration parallel to the density maximum of $(2\bar{1}\bar{1}0)$ poles of titanohematite (Fig. 11). The maximum concentration of amphibole [001] axes might represent a faint mineral lineation; it is noteworthy that it is located at ca. 50° of both K_{max} (Fig. 12) and the concentration of the axes of maximum remanence which is associated to the shape-preferred orientation of magnetite.

In the lineated mylonites, clustered axes of minimum, intermediate and maximum susceptibility correlate well with the strain-induced LPO of titanohematite. K_{min} is close to the maximum concentration of *c*-axes and located close to the pole of the macroscopic foliation plane, and K_{max} is close to the maximum concentration of prism planes pole and sub-parallel to the lineation. In RB614, characterized by a strong macroscopic foliation, the AMS fabric symmetry reflects an axial symmetry around the *c*-axes of titanohematite. Therefore, in all the studied samples, the correlation between AMS fabrics and titanohematite LPO confirms that titanohematite contributes largely to the observed magnetic foliation and/or lineation.

6. Kinematic analysis and fabric strengths

In all but RB614 mylonite samples (Fig. 11), the magnetic lineation (K_{max}) and the maximum concentration of poles to $(2\bar{1}\bar{1}0)$ and $(10\bar{1}0)$ are slightly oblique with respect to the macroscopic stretching lineation (*x*). Such an obliquity between the finite strain axes and the LPO is usually regarded as a potential shear sense indicator (e.g., [8]). The obliquity suggests a dextral sense of shear, for example RB609A, RB538 and RB607A, coherent with macroscopic kinematic indicators observed in the Pádua shear zone [27,35]. An unexpected sinistral shear sense is suggested for RB540, sampled 5 km away from the

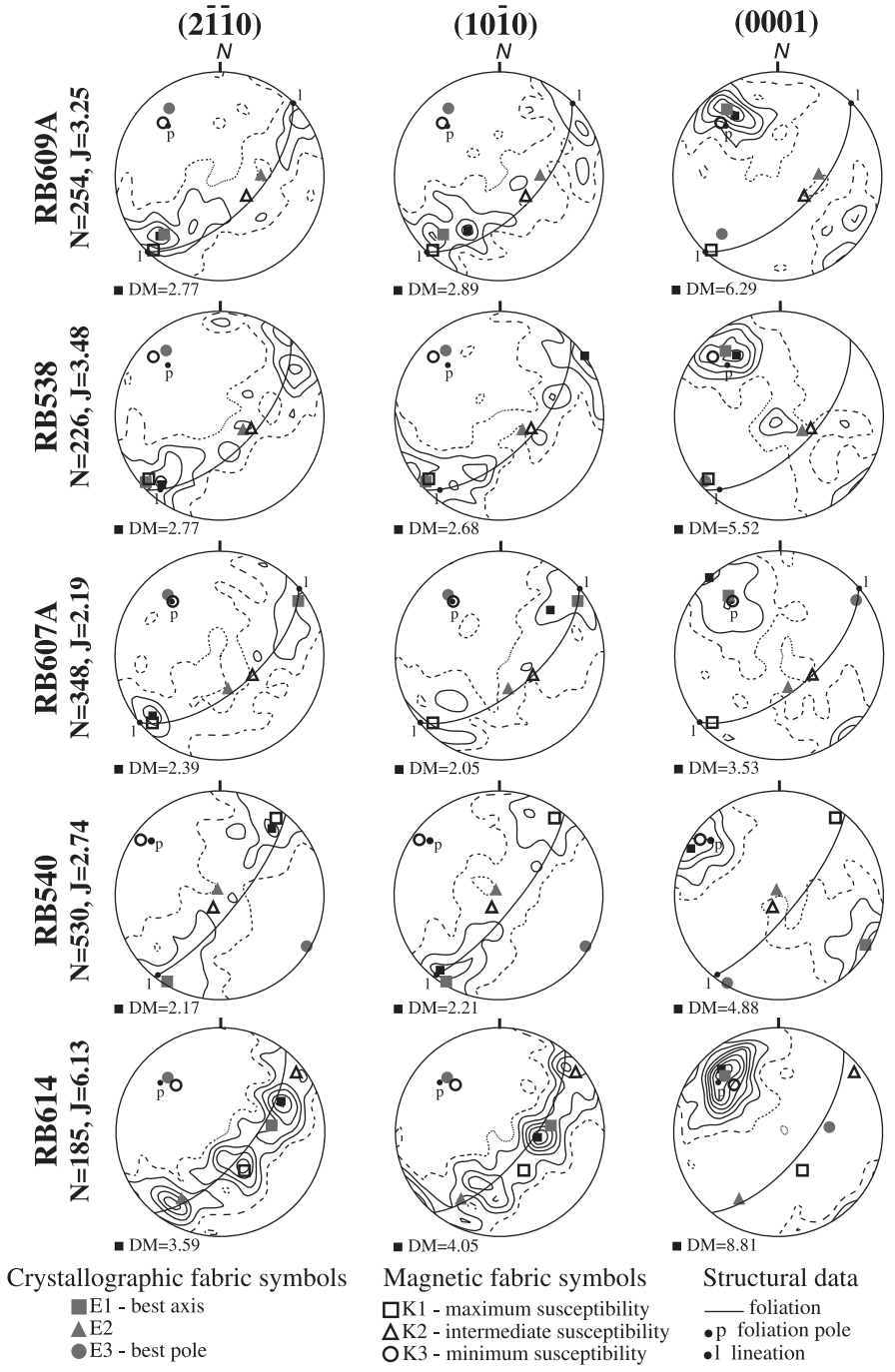

Fig. 11. Titanohematite LPOs from all samples plotted in the geographic reference frame. The mean eigenvectors (K_{max}, K_{int} and K_{min}), and the tectonic foliation and lineation are also plotted. Equal-area projections. Contours at 1, 1.5, 2, 2.5, 3% etc. by 1% area for (2$\bar{1}\bar{1}$0), (10$\bar{1}$0) poles, and at 1, 2, 3% etc. by 1% area for (0001) poles. N, DM as in Fig. 7; J = fabric strength.

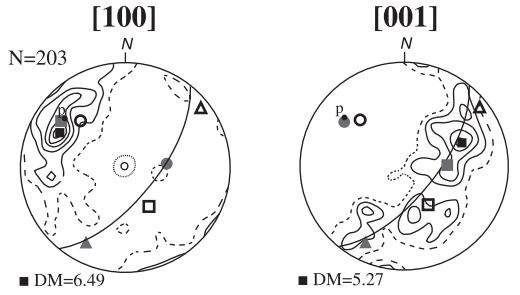

Fig. 12. Amphibole LPO of sample RB614 plotted in the geographic reference frame, equal-area projections. Contours at 1, 2, 3% etc. by 1% area. The mean eigenvectors (K_{max}, K_{int} and K_{min}) are also plotted. p = pole of the tectonic foliation; N, DM as in Fig. 7.

other mylonitic samples. Moreover, the obliquity of the magnetic fabric relative to the structural axes also suggests a sinistral shear. This consistency strengthens the link between the AMS fabric and the LPO of titanohematite.

To compare the magnetic and crystallographic fabric strengths, we have adopted the approach used by Yaouancq and MacLeod [13]. For each crystallographic axis, the eigenvalues $S1 \geq S2 \geq S3$ are calculated from the mean orientation matrix normalized by the number of measurements for each sample. The mean crystallographic fabric parameters L_{LPO} (strength of the titanohematite lineation) and F_{LPO} (strength of the titanohematite foliation) are given by $L_{LPO} = S1/S2$ for $(2\overline{1}\overline{1}0)$, and $F_{LPO} = S1/S2$ for (0001). The strength of the titanohematite fabric ellipsoid axes $R1$, $R2$ and $R3$ is computed from the L_{LPO} and F_{LPO} parameters using $F_{LPO} = R2/R3$, $L_{LPO} = R1/R2$ and $R1+R2+R3 = 1$. Finally, $R1$, $R2$ and $R3$ are used to calculate Jelinek's shape factor: $T_{LPO} = [\ln(R2/R3) - \ln(R1/R2)]/[\ln(R2/R3) + \ln(R1/R2)]$ and the anisotropy degree $P_{LPO} = R1/R3$ (Table 2). Sample RB607A has the weakest LPO of [0001] axes characterized by the lowest J index (2.19). Variations in fabric strengths between lineated mylonites (Fig. 11) may reflect variations in strain intensity across the shear zone. Sample RB607A also displays the less anisotropic crystallographic fabric of titanohematite ($P_{LPO} = 1.71$) and the lowest magnetic anisotropy ($P_{AMS} = 1.51$; Table 1). However, the anisotropy parameters P_{LPO} and P_{AMS} do not show any systematic correlation. This points to other contributions to AMS than titanohematite LPO alone. For instance, the very high degree of magnetic anisotropy ($P_{AMS} = 5.54$) of sample RB538 may be due to the combination of the titanohematite LPO with the shape-preferred orientation of magnetite. This inference is supported by the strong fabric (Fig. 10) of titanohematite, the high mean susceptibility ($K_m = 21.52 \times 10^{-3}$ SI) and the strong AIRM fabric of this sample ($P_{AIRM} > 10$).

Jelinek's parameter T_{LPO} calculated from the titanohematite LPO ranges between 0.24 and 0.94 (Table 2). These positive values correlate with the strong concentration of the [0001] axes. The susceptibility ellipsoid and the crystallographic ellipsoid of all samples present an oblate character (T_{AMS} and $T_{LPO} > 0$), but T_{AMS} (Table 1) and T_{LPO} (Table 2) values do not show any systematic correlation. However, the strongly oblate character of both the susceptibility ellipsoid ($T_{AMS} = 0.81$) and crystallographic ellipsoid of titanohematite ($T_{LPO} = 0.94$) in sample RB614 is in

Table 2
Fabric parameters from titanohematite LPOs

Sample	L_{LPO}	F_{LPO}	P_{LPO}	T_{LPO}	Ellipsoid axes		
					$R1$	$R2$	$R3$
RB538	1.33	1.59	2.14	0.24	0.45	0.34	0.21
RB540	1.17	1.96	2.15	0.62	0.43	0.37	0.20
RB607A	1.18	1.55	1.71	0.53	0.41	0.35	0.24
RB609A	1.17	1.96	2.15	0.62	0.43	0.37	0.20
RB614	1.05	5.00	4.60	0.94	0.46	0.44	0.10

L_{LPO} (strength of the titanohematite lineation), F_{LPO} (strength of the titanohematite foliation), Jelinek's shape parameter T_{LPO} and the anisotropy degree P_{LPO} are defined in the text.

agreement with the sub-planar arrangements of K_{max} and K_{int} in Fig. 6, the well-developed foliation and the lack of visible stretching lineation.

7. Conclusion

Mylonitic fabric in the high-temperature Pádua shear zone is marked by a strong compositional layering that underlines the foliation, and by titanohematite, amphibole and/or orthopyroxene elongated parallel to the macroscopic lineation.

Magnetic foliation and lineation determined from AMS measurements tend to parallel the macroscopic foliation and lineation observed in the field and in hand specimens. Magnetic studies reveal that both para- and ferromagnetic minerals contribute to the AMS. Ti-rich titanohematite (ilmenite), orthopyroxene, amphibole and biotite in variable proportions represent the paramagnetic minerals. Ferromagnetic minerals are mainly iron oxides (Ti-poor titanohematite, magnetite with subordinated pyrrhotite in RB607). The AIRM fabric, due to the shape-preferred orientation of magnetite grains, is coaxial with the AMS fabric.

LPO data show that orthopyroxene, amphibole, biotite and titanohematite have a strong LPO tightly correlated with the tectonic fabric. Among these minerals, titanohematite is the only mineral present in relatively large proportions ($>1.5\%$) in all studied granulitic mylonites. The LPO of titanohematite is characterized by the preferential orientation of (0001) poles sub-perpendicular to the foliation and by the poles of the prism planes in the foliation plane, which define a girdle containing a maximum concentration close to the lineation in the lineated mylonites. This characteristic LPO likely results from plastic deformation of titanohematite through slip on (0001) planes.

For the studied mylonites, a good correlation is observed between the AMS ellipsoid axes and the LPOs of titanohematite: the axis of minimum susceptibility (K_{min}) is close to the maximum concentration of *c*-axes, and the axis of maximum susceptibility (K_{max}) is close to the maximum concentration of poles of the prism planes. These clear relationships between the AMS axes and the strain-induced LPO of titanohematite provide a strong constraint on the tectonic significance of the measured magnetic fabric. On the other hand, no clear correlation has been established between the intensity of AMS and the fabric strength calculated from the LPO of titanohematite. This lack of correlation highlights that the magnitude and shape of the finite strain ellipsoid cannot be evaluated from AMS measurements when various minerals contribute to the magnetic susceptibility.

In non-mylonitic granulites, it is frequently impossible to measure the tectonic fabric. AMS measurement allows fast and reliable mapping of the magnetic foliation and lineation. Since under high-temperature conditions, titanohematite develops a clear LPO through dislocation creep, measurement of its LPO provides a strong constraint on the magnetic properties of tectonites and the deformation they have undergone. Titanohematite LPO therefore represents a reliable guide for tectonic interpretation of AMS measurements.

Acknowledgements

We would like to thank D. Mainprice for providing crystallographic fabric analysis programs and for fruitful discussions. We also thank L. Lagoeiro for providing the hematite ore sample and C. Nevado for the ultra-polished thin sections. J.L. Bouchez, F. Boudier and G.E. Lloyd are gratefully acknowledged for their helpful reviews. The crystal orientation measurements were made using the EBSD/SEM system at Laboratoire de Tectonophysique, Université Montpellier II funded by grants from CNRS/INSU, UMII, NSF Project #EAR-9526840 'Anatomy of an Archean Craton' and ISTEEM. Composition analyses were made using the SEM-EDS system at Instituto de Geociências, Universidade de São Paulo. The authors thank CAPES (Project: 287/99), FAPESP (Projects: 95/8399-0 and 95/0283-2) and CNPq/CNRS (Project: 910144/98-2) for financial support. *[AC]*

References

[1] F. Hrouda, Magnetic anisotropy of rocks and its application in geology and geophysics, Geophys. Surv. 5 (1982) 37–82.

[2] P. Rochette, M. Jackson, C. Aubourg, Rock magnetism and the interpretation of anisotropy of magnetic susceptibility, Rev. Geophys. 30 (1992) 209–226.

[3] G.J. Borradaile, B. Henry, Tectonic applications of magnetic susceptibility and its anisotropy, Earth Sci. Rev. 42 (1997) 49–93.

[4] R.I.F. Trindade, M.I.F. Raposo, M. Ernesto, R. Siqueira, Magnetic susceptibility and partial anhysteretic remanence anisotropies in the magnetite-bearing granite pluton of Tourão, NE Brazil, Tectonophysics 314 (1999) 443–468.

[5] M.I.B. Raposo, M.S. D'Agrella-Filho, Magnetic fabrics of dike swarms from SE Bahia State, Brazil: their significance and implications for Mesoproterozoic basic magmatism in the São Francisco Craton, Precambrian Res. 99 (2000) 309–325.

[6] M. Jackson, Anisotropy of magnetic remanence: a brief review of mineralogical sources, physical origins and geological applications, and comparison with susceptibility anisotropy, Pure Appl. Geophys. 136 (1991) 1–28.

[7] D.H. Tarling, F. Hrouda, The Magnetic Anisotropy of Rocks, Chapman and Hall, London, 1993, 217 pp.

[8] J.L. Bouchez, A. Nicolas, G. Lister, Fabric asymmetry and shear sense in movement zones, Geol. Rund. 72 (1983) 401–419.

[9] A. Nicolas, J.L. Bouchez, F. Boudier, Interprétation cinématique des déformations plastiques dans le massif de lherzolites de Lanzo, Tectonophysics 14 (1972) 143–171.

[10] P. Blumenfeld, J.L. Bouchez, Shear criteria in granite and migmatite deformed in the magmatic and solid states, J. Struct. Geol. 10 (1988) 361–372.

[11] G.J. Borradaile, Magnetic susceptibility, petrofabric and strain, Tectonophysics 156 (1988) 1–20.

[12] K. Benn, P. Rochette, J.L. Bouchez, K. Hattori, Magnetic susceptibility, magnetic mineralogy and magnetic fabrics in a late Archean granitoid-gneiss belt, Precambrian Res. 63 (1993) 59–81.

[13] G. Yaouancq, C.J. MacLeod, Petrofabric investigation of gabbros from the Oman ophiolite: comparison between AMS and rocks fabric, Mar. Geophys. Res. 21 (2000) 289–305.

[14] F. Hrouda, H. Siemes, N. Herres, C. Hennig-Michaeli, The relationship between the magnetic anisotropy and the c-axis fabric in a massive hematite ore, J. Geophys. 56 (1985) 174–182.

[15] H.G. Brokmeier, Neutron diffraction texture analysis of multi-phase systems, Textures Microstruct. 10 (1989) 325–345.

[16] G. Will, P. Schäfer, P. Merz, Texture analysis by neutron diffraction using a linear position sensitive detector, Textures Microstruct. 10 (1989) 375–387.

[17] H. Siemes, H. Schaeben, C.A. Rosière, H. Quade, Crystallographic and magnetic preferred orientation of hematite in banded iron ores, J. Struct. Geol. 22 (2000) 1747–1759.

[18] D. Mainprice, G. Lloyd, M. Casey, Individual orientation measurements in quartz polycrystals: advantages and limitations for texture and petrophysical property determinations, J. Struct. Geol. 15 (1993) 1169–1187.

[19] G.E. Lloyd, D.J. Prior, EBSD technique and application in geosciences, Göttinger Arb. Geol. Paläontol. Sb4 (1999) 112–113.

[20] Y. Hasui, C.D.R. Carneiro, A.M. Coimbra, The Ribeira folded belt, Rev. Bras. Geoci. 5 (1975) 257–266.

[21] R. Trompette, Geology of Western Gondwana (2000–500 Ma), Balkema, Rotterdam, 1994, 350 pp.

[22] A. Vauchez, A. Tommasi, M. Egydio-Silva, Self-indentation of continental lithosphere, Geology 22 (1994) 967–970.

[23] C. Porcher, L. Fernandes, M. Egydio-Silva, A. Vauchez, Dados preliminares do metamorfismo M1 da Faixa Ribeira: Região de Três Rios e Santo Antônio de Pádua (RJ), in: V Simpósio Nacional de Estudos Tectônicos, Gramado, Brasil, 1995, pp. 71–73.

[24] F. Söllner, B. Lammerer, K. Weber-Diefenbach, Die Krustenentwicklung in der Kustenregion nordlich von Rio de Janeiro/Brasilien, Münch. Geol. Helfe 4 (1991) 1–101.

[25] N. Machado, C. Vallares, M. Heilbron, C. Valeriano, U-Pb geochronology of the central Ribeira belt (Brazil) and implications for the evolution of the Brazilian Orogeny, Precambrian Res. 79 (1996) 347–361.

[26] H.K. Brueckner, D. Cunningham, F.F. Alkmin, S. Marshak, Tectonic implications of Precambrian Sm-Nd dates from the southern São Francisco craton and adjacent Araçuaí and Ribeira belts, Brazil, Precambrian Res. 99 (2000) 255–269.

[27] M. Egydio-Silva, A. Vauchez, J. Bascou, J. Hippertt, High temperature deformation in the Neoproterozoic transpressional Ribeira belt, southeast Brazil, Tectonophysics (2001) in press.

[28] M.I.B. Raposo, M. Egydio-Silva, Magnetic fabric studies of high-grade metamorphic rocks from the Juiz de Fora Complex, Ribeira belt, SE Brazil, Int. Geol. Rev. 43 (2001) 441–456.

[29] V. Jelinek, Characterization of the magnetic fabrics of rocks, Tectonophysics 79 (1981) 63–67.

[30] C. Constable, L. Tauxe, The bootstrap for magnetic susceptibility tensor, J. Geophys. Res. 95 (1990) 8383–8395.

[31] G.E. Lloyd, N.H. Schmidt, D. Mainprice, D.J. Prior, Crystallographic textures, Mineral. Mag. 55 (1991) 331–345.

[32] D.J. Dingley, D.P. Field, Electron backscatter diffraction and orientation imaging microscopy, Mater. Sci. Technol. 13 (1997) 69–78.

[33] N.C. KriegerLassen, The relative precision of crystal orientations measured from electron backscattering patterns, J. Microsc. 181 (1996) 72–81.

[34] C.A. Rosière, H. Quade, H. Siemes, F. Chemale Jr., Fab-

ric, texture and anisotropy of magnetic susceptibility in high-grade iron ores from the Quadrilátero Ferrífero, Minas Gerais, Brazil, Mater. Sci. Forum 273–275 (1998) 693–700.
[35] M. Egydio-Silva, D. Mainprice, Determination of stress directions from plagioclase fabrics in high grade deformed rocks (Além Paraiba shear zone, Ribeira fold belt, southeastern Brazil), J. Struct. Geol. 21 (1999) 1751–1771.
[36] S.M. Agar, G.E. Lloyd, Deformation of Fe-Ti oxides in gabbroic shear zones from the Mark area, Proc. ODP Sci. Results 153 (1997) 123–140.
[37] C.A. Rosière, H. Siemes, H. Quade, H.-G. Brokmeier, M. Jansen, Microstructures, textures and deformation mechanisms in hematite, J. Struct. Geol. 23 (2001) 1429–1440.
[38] H. Siemes, B. Klingenberg, G. Dresen, E. Rybacki, M. Nauman, W. Schäfer, E. Jansen, C.A. Rosière, Experimentally and naturally deformed hematite ores, in: VII Simpósio Nacional de Estudos Tectônicos, Lençois, Brasil, 1999, pp. 59, Sessão 5.
[39] T. Bretheau, J. Castaing, J. Rabier, P. Veyssière, Mouvement des dislocations et plasticité à haute température des oxydes binaires et ternaires, Adv. Phys. 28 (1979) 829–1014.
[40] C. Hennig-Michaeli, Microscopic structure studies of experimentally and naturally deformed hematite ores, Tectonophysics 39 (1977) 255–271.
[41] H. Siemes, C. Hennig-Michaeli, Ore minerals, in: H.-R. Wenk (Ed.), Preferred Orientation in Deformed Metals and Rocks: An Introduction to Modern Texture Analysis, Academic Press, New York, 1985, pp. 335–358.
[42] N.H. Woodcock, M.A. Naylor, Randomless testing in three-dimensional orientation data, J. Struct. Geol. 5 (1983) 539–548.
[43] H.J. Bunge, Texture Analysis in Materials Sciences, Butterworths, London, 1982, 593 pp.
[44] C.J. Archanjo, P. Launeau, J.L. Bouchez, Magnetic fabric vs. magnetite and biotite shape fabrics of the magnetite-bearing granite pluton of Gameleiras (Northeast Brazil), Phys. Earth Planet. Inter. 89 (1995) 63–75.
[45] V. Grégoire, J. Darrozes, P. Gaillot, A. Nédélec, P. Launeau, Magnetite grain shape fabric and distribution anisotropy vs rock magnetic fabric: a three-dimensional case study, J. Struct. Geol. 20 (1998) 937–944.
[46] Y. Uyeda, M.D. Fuller, J.C. Belshé, R.W. Girdler, Anisotropy of magnetic susceptibility of rocks and minerals, J. Geophys. Res. 68 (1963) 279–291.